A Glucose Biosensor Using CMOS Potentiostat and Vertically Aligned Carbon Nanofibers

Khandaker A. Al Mamun, *Student Member, IEEE*, Syed K. Islam, *Senior Member, IEEE*, Dale K. Hensley, and Nicole McFarlane, *Member, IEEE*

***Abstract*—This paper reports a linear, low power, and compact CMOS based potentiostat for vertically aligned carbon nanofibers (VACNF) based amperometric glucose sensors. The CMOS based potentiostat consists of a single-ended potential control unit, a low noise common gate difference-differential pair transimpedance amplifier and a low power VCO. The potentiostat current measuring unit can detect electrochemical current ranging from 500 nA to 7 μA from the VACNF working electrodes with high degree of linearity. This current corresponds to a range of glucose, which depends on the fiber forest density. The potentiostat consumes 71.7 μW of power from a 1.8 V supply and occupies 0.017 mm^2 of chip area realized in a 0.18 μm standard CMOS process.**

***Index Terms*—Amperometry, glucose monitoring, potentiostat, transimpedance amplifier, vertically aligned carbon nanofibers.**

I. Introduction

REAL time glucose monitoring schemes to control glycemic levels impacts diabetic outcomes, such as improved hemoglobin A1C levels and reduced long term micro and macrovascular complications [1], [2]. Diabetes can cause episodes of hypo or hyperglycemia where blood glucose levels are below or above the healthy plasma glucose limit of 80 to 130 mg/dl (4.44 to 7.22 mM) before a meal or less than 180 mg/dl (10 mM) in an hour following the meal [3]. A real time glucose monitoring system needs to be compact, power-efficient, realizable in a portable system, sensitive, and linear for the target dynamic range. Enzymatic sensors are popular choices in glucose monitors [4]–[6]. The addition of chemically stable nanostructures in the sensor can significantly improve sensor sensitivity [7]–[9]. Vertically aligned carbon nanofibers (VACNF) have the unique capability of high loading of catalyst, effective enzyme binding and increased detection sensitivity [10]. VACNFs are also chemically stable and are capable of detecting a wide range of target chemicals with the appropriate functionalization. We have previously demonstrated the VACNF platform in highly sensitive glucose sensing [10], [11].

Manuscript received October 7, 2015; revised January 28, 2016 and March 31, 2016; accepted April 12, 2016. Date of publication June 22, 2016; date of current version July 26, 2016. This work was supported in part by the Office of Basic Energy Sciences, U.S. Department of Energy at the Center for Nanophase Materials Science (CNMS), Oak Ridge National Laboratory. This paper was recommended by Associate Editor J. Blain Christen.

K. A. Al Mamun, S. K. Islam, and N. McFarlane are with the Electrical Engineering and Computer Science Department, University of Tennessee, Knoxville, TN 37996 USA (e-mail: kmamun@vols.utk.edu).

D. K. Hensley is with the CNMS division, Oak Ridge National Laboratory, Oak Ridge, TN 37831 USA.

Color versions of one or more of the figures in this paper are available online at http://ieeexplore.ieee.org.

Digital Object Identifier 10.1109/TBCAS.2016.2557787

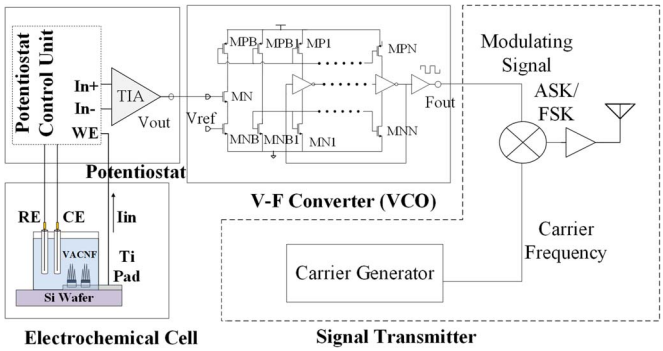

Fig. 1. General overview of the CMOS potentiostat based amperometric glucose monitoring system.

Potentiostats are used for constant voltage amperometry, cyclic voltammetry, or impedance spectroscopy in three-electrode electrochemical measurements [12]–[16]. Among these schemes the amperomtric biosensors are a popular choice [10], [17], [18]. Many enzyme functionalized working electrodes must maintain a negative potential with respect to the reference electrode. This limits the use of grounded counter electrode potentiostats in amperometric glucose sensors [12]. For electrochemical current measurement, a transimpedance amplifier (TIA) is required. Among the available topologies, fully differential potentiostat topologies demonstrate higher dynamic range in low voltage processes [14], [20], while linearity errors in current mirror based potentiostats have been improved using error cancellation loops or compensation networks [21], [22]. Current potentiostats offer wide dynamic range and improved sensitivity in the pA and fA range using capacitor charging time, switched capacitor circuits, sigma-delta ADCs, or semi-synchronous sigma-delta ADCs at the cost of power ($\sim$mW) and chip area ($\sim$60 000 μm^2) [17], [23]–[25]. Low power, compact potentiostat topologies using bulk driven amplifiers, or simple feedback TIA structures have been adopted to realize power and area efficient topologies [26], [27].

This paper reports a highly linear, low power, compact potentiostat with a single ended potential control unit, a difference-differential current measuring unit and a current starved low power VCO for integration with VACNF enzymatic glucose sensors (Fig. 1). The VCO is employed to convert the sensor response to a signal, which can be directly transmitted using modulation by a carrier signal. The VCO integration enables improved efficiency of low power implementation and reduced area compared to using ADC/I-F converters to directly convert sensor currents to FSK signals [20], [28]. The proposed potentiostat sensing system achieves competitive performance (high

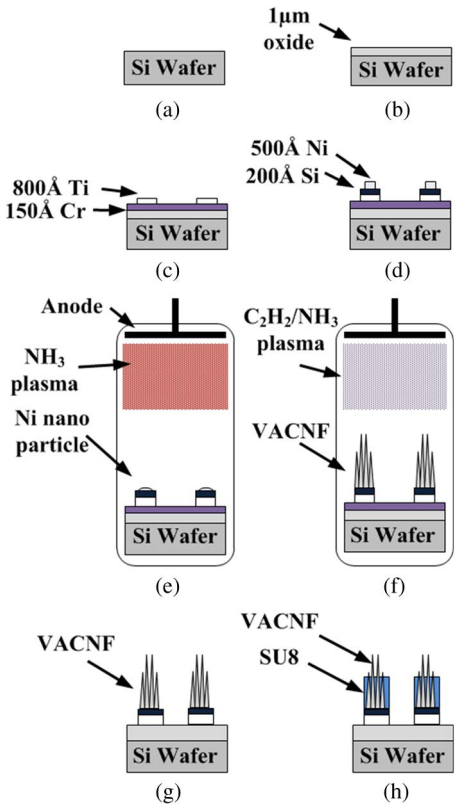

Fig. 2. VACNF growth process. (a) Si substrate. (b) Oxidation of Si wafer to form 1 μm thick SiO_2, e-beam evaporation of (c) 150 Å Cr and 800 Å Ti. (d) 200 Å Si and 500 Å Ni on predetermined nanofiber growth positions. (e) Formation of Ni nanoparticle with NH_3 plasma in PECVD. (f) Growth of VACNF in C_2H_2/NH_3 plasma. (g) Dry etch of conductive Cr layer. (h) SU8 coating on the VACNF surface for increased fiber strength.

CMRR, high SFDR, increased linearity and high sensitivity) at significantly lower power consumption compared to the potentiostats reported in literature.

We have previously reported simulation results of a TIA topology [19] and have separately optimized the VACNF nanofabrication and testing process using commercial benchtop instrumentation. This work represents an expanded treatment of [29] and reports on the redesigned TIA topology and its integration with the potentiostat control unit and the VACNF working electrode. Additionally, we report on sensor modeling and verify the two-chip sensing solution with glucose. This work represents the first demonstrated results of VACNF electrochemical working electrodes with CMOS readout circuitry in an integrated two-chip platform scheme.

The paper is organized as follow, the role of the VACNF as working electrodes is discussed in Section II, while the potentiostat design is presented in Section III. The experimental results are presented in Section IV and the conclusion is summarized in Section V.

II. VACNF as Working Electrodes

DC plasma-enhanced chemical vapor deposition (PECVD) was employed to synthesize the VACNF fiber forests on silicon wafer (Fig. 2). The VACNF fabrication process adopted for our specific application is based on the work by Melechko *et al.* [30]. A 150 Å layer of Cr was deposited on the silicon wafer, which acted as the cathode in the PECVD process. A 300 Å Ti layer was deposited on the wafer to form the interconnects. All interconnects are terminated to a Ti metal island occupying an area of 300 μm $\times$ 300 μm, where 5 μm Ni dots were patterned with pitches of 15 μm, 20 μm, and 30 μm, respectively. The Ni dots defined the locations of the VACNF growth, and dot sizes below a critical diameter (100 nm) resulted in the growth of single fibers.

For increased fiber redundancy, a Ni dot size of 5 μm was chosen. This resulted in forests of fibers, multiple fibers on a single predefined spot. Acetylene (75 sccm) and ammonia gas (200 sccm) were injected into the PECVD chamber while the chamber temperature was increased to 700 °C. Pressure was controlled at 15 Torr. The reaction time determined the height of the fiber and a duration of approximately 20 to 25 minutes was chosen for an approximate VACNF height of 20 to 25 μm. The plasma power was 480 W. The Cr layer was etched following the VACNF growth leaving only the VACNF forests and the Ti interconnects on the wafer. The VACNF surface was coated with a thin SU8 layer, which was etched away from the VACNF tips with buffered hydrofluoric acid (HF or BOE 6:1). This surface modification improves electrode reusability in the electrochemical cell. The SU8 2005 coating can be formed up to a maximum height of 8 μm. The uncoated bare surface areas of the forest are active sites for electrochemical reactions and are proportional to the electrochemical current. VACNF forest heights taller than 25 μm resulted in a weak mechanical structure. Thus, based on the experimental data, we chose an optimum height of 20 to 25 μm to leverage the maximum sensor active area without sacrificing robustness of the overall structure.

VACNFs have many irregularities and active sites throughout its surface, which allows for strong adsorption of enzymes. The structural robustness and high conductivity of the VACNF electrodes offer direct transfer of charge from electrochemical reaction centers to the external readout circuits [10], [30]. The density of the VACNF forest in an electrode is related to the sensor sensitivity. Use of high density VACNF forests in highly sensitive glucose sensing is prone to diffusion limited currents. As such low density VACNF forests electrodes are better suited for detecting large concentrations of glucose [11]. To detect a wide range of glucose, electrodes having different VACNF forests densities can be used on the same platform. In this work four Ti working electrodes, each having an area of 300 μm $\times$ 300 μm, were fabricated with varying VACNF forest densities containing 225, 400, and 900 VACNF forests, respectively. Fig. 3(a) shows a working electrode (WE) with 900 VACNF forests. We have previously demonstrated that bare nanofibers lose their mechanical integrity in repeated tests. The robustness of the fibers is increased by coating them with SiO_2 and/or SU8. We have experimentally verified that the usage of SU8 coating results in the best overall long time response [31]. Fig. 3(b) shows the SU8 coated WE.

To characterize the VACNF electrodes, a CHI 660D electrochemical analyzer was used. 2.5 mM of ruthenium hexamine trichloride $(Ru(NH_3)_6Cl_3)$ in 0.1 M KCl solution was used to characterize the electrodes. The peak current in the electrochemical reaction is proportional to the reaction sites available

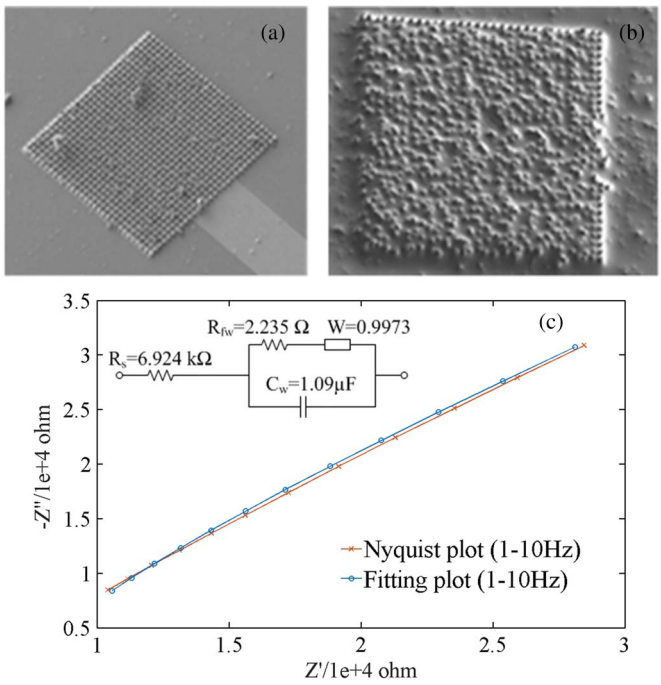

Fig. 3. (a) VACNF on Ti forming the working electrodes. (b) SU8 coated WE. (c) Nyquist plot of the enzyme functionalized VACNF electrode (frequency < 10 Hz) and electrical equivalent model of VACNF microelectrode in 5 mM glucose solution (inset).

on the surface of the electrode. Electrodes containing 225, 400, and 900 VACNF forest show cathodic peak currents of 0.09 μA, 0.16 μA, and 0.219 μA, respectively. In order to realize a glucose sensor system incorporating the proposed potentiostat readout, the VACNF electrodes were functionalized with an enzyme [glucose oxidase (GOx)] and a co-enzyme [horseradish peroxide (HRP)]. GOx oxidizes glucose resulting in gluconic acid and produces hydrogen peroxide (H_2O_2) as a byproduct. HRP facilitates reduction of hydrogen peroxide in the electrolyte enriched solution. The electrons necessary for the reduction reaction are supplied by the working electrode of the electrochemical cells. The reaction is outlined below.

$$\begin{aligned} &\text{Glucose} + O_2 \xrightarrow{GO_x} \text{Gluconic acid} + H_2O_2 \\ &H_2O_2 + 2H^+ + 2e^- \xleftrightarrow{\text{HRP}} 2H_2O. \end{aligned} \tag{1}$$

The peak current in the reduction reaction occurs when the working electrode potential reaches -0.78 V with reference to the reference electrode. 5 μL of HRP and 5 μL GOx were spread over the VACNF islands, and air-dried for 10 hours inside a biohood. The enzyme functionalized VACNFs were then stored in PBS at 4 °C.

There are various models available for VACNF fibers which demonstrate a strong relationship between the nanofiber density and the electrochemical sensitivity [32], [33]. A single nanoelectrode exhibits a high signal-to-noise ratio, which makes it useful for ultrasensitive biomolecule detection. However, high density VACNF fibers leads to macroelectrode behavior with anodic and cathodic peak currents and background charging-discharging currents [33]. Overlaps of the radial diffusion layers of the neighboring VACNF fibers are prominent in high density fibers. This work uses fiber forests to implement a macroscale electrode with moderate sensitivity to enable operation within the diffusion limit. The forests are distributed such that there is no interaction between the radial diffusion layers of the neighboring forests.

The VACNF forest in a solution can be modeled by a lumped RC network in series-parallel configuration. Previously, single carbon nanofibers have been modeled with a Randles cell, representing a single time constant. However, after SU8 and enzyme coating are applied the cell's properties changes. The porosity of the carbon nanofiber presents a large surface area for charge transfer giving rise to a large capacitance and a diffusion impedance, i.e., a Warburg impedance. Fig. 3(c) shows a Nyquist plot of the impedance measurement of an enzyme functionalized carbon nanofiber electrode in 5 mM glucose solution using the CHI 660D electrochemical analyzer. From the Nyquist plot, it is obvious that both kinetic and diffusion processes are dominant in the VACNF electrochemical cell. The model consists of a solution resistance, a double-layer capacitance, a charge transfer or polarization resistance, and a Warburg impedance. For frequencies greater than 100 Hz, the Nyquist plot resembles Randles cell and demonstrates lower charge transfer resistances $(\sim\Omega)$ and low capacitance (nF) compared to similar size platinum electrodes $(\sim\text{k}\Omega)$ [34]. For frequencies less than 10 Hz, the Nyquist plot is a diagonal line corresponding to a solution resistance of 6.92 kΩ with a Warburg impedance and a high double-layer capacitance (μF).

A nonlinear least square-fitting algorithm in the CHI660D electrochemical analyzer was used to generate the empirical model of the VACNF. The algorithm takes an initial value and optimizes the parameters for the entire frequency spectrum. For a wide frequency spectrum the algorithm gives poor fitting due to the uncertainty of an initial value which can converge for the entire frequency range. The amperometric device under consideration works in the range of 0.1 to 10 Hz. The VACNF microelectrode demonstrates a non-planar diffusion profile, which enhances the diffusion process compared to a planar electrode. The Warburg elements represent the diffusion related impedance, which are frequency dependent and show a large impedance in Nyquist plot at low frequency. The range of parameters for the different VACNF architectures are double-layer capacitances of 0.8 to 2 μF, Faradaic resistances of 2 to 466 Ω and Warburg constant around 0.99. In this work we have used a 900 VACNF forest electrode configuration and have only reported the model parameter for that particular electrode architecture. The VACNF microelectrodes, thus, present very low charge transfer resistances (testing frequency < 10 Hz) and exhibit high double layer capacitances resembling a macroelectrode behavior in an electrochemical setup. Based on the VACNF forest density on the working electrode, the electrochemical current can be as small as tens of nA with background currents of 3 μA, and electrode capacitances as large as 100 μF [11]. The background current is the steady state current flowing in the blank/buffer solution [typically PBS for benchtop measurements can be considered as the DC offset current in the potentiostat current measuring unit (TIA)]. Thus, VACNF sensors require a low-noise frontend and need to accommodate the DC offset due to the background current and should demonstrate stable operation over the entire range of electrode capacitances.

III. Potentiostat Design

Potentiostat circuits for amperometric measurements typically use three electrodes: a working electrode (WE), an auxiliary/counter electrode (AE or CE) and a reference electrode (RE). The working electrode is functionalized with enzymes to provide specificity for the analyte under consideration. The electrochemical reaction occurs at the functionalized electrode when a constant potential difference is maintained across the reference and the working electrodes. The current source/sink from the working electrode is supplied by the counter electrode and thus the reference electrode maintains a fixed potential throughout the reaction.

In the proposed glucose sensing system, the VACNFs act as the working electrode, while a standard Ag/AgCl electrode is used as the reference and the counter electrodes (Fig. 1). The potentiostat consists of two major units: 1) the potential control unit and 2) the electrochemical current measuring unit with a frequency translation unit for data transmission. We have studied two potential control units in this paper: 1) an amplifier based potential control unit where the WE is directly coupled with current measuring unit and 2) a current regulator based control unit where the change in currents are well-regulated during coupling. The electrochemical current is coupled to the transimpedance amplifier through a current mirror. A difference common gate input pair differential transimpedance amplifier follows the potential control unit and converts the cell currents into voltages. The common gate difference input stage presents a low noise frontend interface. A low power current starved standard VCO follows the transimpedance amplifier to convert the measured voltage to baseband frequencies.

A. Potential Control Unit

The control unit in the potentiostat maintains a constant potential at the reference electrode specified by the control voltage, and sources current at the counter electrode as needed to support the current flow through the working electrode. The VACNF electrochemical sensor can be modeled as shown in Fig. 4, where R_{S1} and R_{S2} are solution resistances, $R_{\rm fw}$ is the Faradaic resistance of the working electrode, $R_{\rm fc}$ is the Faradaic resistance of the counter electrode, C_W is the total (double layer and specific) capacitance of the working electrode, C_C is the double layer capacitance of the counter electrode, $Z_{\rm RE-CE}$ is the net impedance in between the counter and the reference electrodes and $Z_{\rm RE-WE}$ is the net impedance in between the reference and the working electrodes. The impedances in the electrochemical cell thus can be expressed as

$$Z_{\rm CE-RE} = R_{S1} + \left(R_{\rm fc} \| \frac{1}{\rm sC_C}\right)$$
$$Z_{\rm RE-WE} = R_{S2} + \left(R_{\rm fw} \| \frac{1}{\rm sC_W}\right). \quad (2)$$

Typically $R_{\rm fw} \gg R_{\rm fc} \gg R_{S1}$ & R_{S2}, and $C_W \gg C_C$. As such, at low frequencies the Faradaic resistances dominate and at high frequencies the double layer capacitances control the net impedance. The transfer function of the amplifier based single-ended potential control unit [Fig. 4(a)] with the electrochemical cell can be expressed as established in [14]

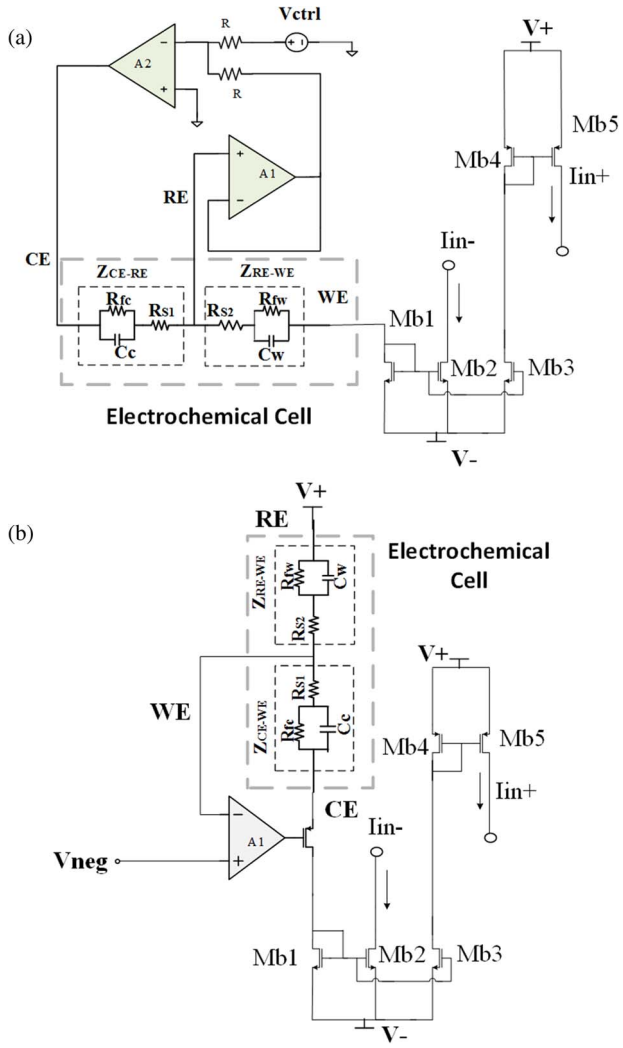

Fig. 4. Potentiostat control unit. (a) Amplifier based control unit. (b) Current regulator based control unit.

$$\frac{V_{\rm RE-WE}}{V_{\rm ctrl}} = \frac{A_2 Z_{\rm RE-WE}}{A_2 Z_{\rm RE-WE} + 2(Z_{\rm RE-WE} + Z_{\rm CE-RE})} \quad (3)$$

where $V_{\rm RE-WE}$ is the voltage across the reference and the working electrodes, $V_{\rm CE-RE}$ is the voltage across the counter and the reference electrodes, A_2 is the open loop gain of the amplifier and $V_{\rm ctrl}$ is the control voltage. For a high A_2, the equation reduces to $V_{\rm RE-WE} = V_{\rm ctrl}$ and the voltage between the reference and the working electrodes tracks the control voltage.

The amplifier A_2 controls the current in the feedback path, while A_1 is a voltage follower which ensures high impedance at the reference electrode. Current generated at the working electrode due to the electrochemical reaction is supplied by the counter electrode. All current sources and loads in the control unit have been optimized for low power operation using the inversion coefficient method [35]. The single ended potential control unit uses an amplifier with single ended output to control the cell potential as opposed to a fully differential amplifier, which uses a differential output to control the cell

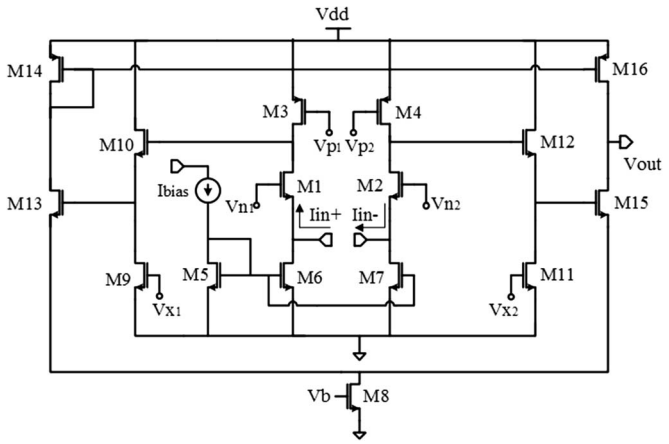

Fig. 5. Potentiostat current measuring unit difference-differential transimpedance amplifier.

potential. One disadvantage of this single ended unit is that at high current levels the diode connected transistor Mb1 causes a nonlinear response. An alternative method involves use of a current regulator based control structure [Fig. 4(b)]. Both the WE and the RE are well regulated in this topology at a fixed potential due to the feedback. V_{RE-WE} is well maintained in this topology and provides better linearity. In this work, both the potential control structures were fabricated and tested with the proposed system (Fig. 4).

B. Current Measuring Unit

Typically the sensor current generated in the potentiostat is measured using a feedback TIA. The inductive nature of traditional feedback TIA can be attributed from the following equation:

$$Z_{\text{in}} = \frac{R_F}{A(s)+1} \tag{4}$$

where Z_{in} is the input impedance of the feedback TIA, R_F is the feedback resistor, and A(s) is the amplifier open loop gain. At low frequencies, the input impedances are quite small. While at higher frequencies, the degradation of the amplifier loop gain results in a net increase in impedance. The transfer characteristic of the feedback TIA thus resembles an inductive load. On the other hand, the input impedance of a common-gate input stage TIA (Fig. 5) with current mirror is simply $1/g_{\text{Mb1}} \| 1/\text{sC}_{\text{in}}$, where g_{Mb1} is the transconductance of transistor Mb1 (Fig. 4) and C_{in} is the net capacitances at the gate. The dependence of the input impedance on frequency can be expressed as

$$\text{As } s \to 0, \text{Zin} \approx \frac{1}{g_{\text{Mb1}}} \text{ and } s \to \infty, \text{Zin} \approx 0. \tag{5}$$

Thus, the input impedance decreases as the frequency increases and the current mirror isolating the control unit from the TIA improves the stability of the potentiostat circuit. In addition, to achieve minimum distortion at the amplified signal, the capability of a differential structure to suppress even harmonic components can be implemented in the TIA. Thus, the output of the common gate difference stage was followed by a differential stage to take advantage of the aforementioned features. The schematic of the TIA based on the topology in [19] is shown in Fig. 5. The transimpedance amplifier has been optimized by tradeoffs in noise, power, dynamic range, layout area, gain, and bandwidth utilizing the inversion coefficient method, which enables selection of MOS inversion levels according to the design requirements.

C. Optimization of the TIA Structure

The circuit schematic of the difference-differential pair transimpedance amplifier is shown in Fig. 5. The first stage is represented by a common gate difference pair, which is formed by transistors M1-M7. As the VACNF amperometric sensor can have background currents as high as 3 μA, the first stage of the amplifier was biased with a current source of at least three times the input current. For this particular application, a bias current of 10 μA was chosen. The outermost stage is a differential stage comprised of transistors M8, M13-M16, and is connected to the input difference stage through a level shifter pair consisting of transistors M9-M12. The net power consumption of the structure is $P = V_{\text{dd}} \times (2I_{\text{bias}} + 2I_{\text{SF}} + I_{\text{tail}})$, where I_{bias} is the first stage bias current, I_{SF} is the bias current of the level shifter and I_{tail} is total current of the outer differential stage. To keep the net power consumption low, the outer differential stage was biased with much lower current (500 nA) compared to the first stage.

Corruption of the electrochemical signal by interfering noise sources can limit the use of a potentiostat in sensitive sensing application. The signal-to-noise ratio, a measure of the potentiostat's immunity to noise sources, is calculated similar to [14]. The average mean square value of the current $(\overline{i_n^2})$ and the voltage noise sources $(\overline{v_n^2})$ are replaced by the MOSFET flicker and thermal noise expressions. See (6), shown at the bottom of the page, where, I_f is the electrochemical current, W and L are the width and length of the transistor, C_{ox} is the oxide capacitance, f is the frequency, r_1 is the load resistance of the common-gate stage, and is $r_{03/04}$ (the drain-source resistances of the transistor M3/M4), K_f is the process dependent flicker noise constant, T is temperature, k is Boltzmann's constant, and g_m is the device transconductance. The input common gate difference pair primarily contributes to the TIA noise while for the outer stages the noise contributions are negligible due to the high input stage gain. The net DC gain of the TIA can be expressed as

$$A_{\text{vi}} = g_{m16} r_{O16} \left[\frac{g_{m13}/g_{m14}}{1 + g_{m13} r_{O8}} \cdot (r_{O3} \| r_{O1}) \cdot \frac{g_{m10} r_{O9}}{1 + g_{m10} r_{O9}} \right] + r_{O16} \left[\frac{g_{m15}}{1 + g_{m15} r_8} \cdot (r_{O4} \| r_{O2}) \cdot \frac{g_{m12} r_{O11}}{1 + g_{m12} r_{O11}} \right] \tag{7}$$

$$\text{SNR} = \frac{I_f^2}{8\text{kT}\left[\frac{2}{3}(g_{m6,7} + g_{\text{Mb6,Mb2}}) + \frac{1}{r_1}\right] + \frac{2K_f}{\text{Cox}.f}\left[\frac{g_{m6,7}^2}{(\text{WL})_{6,7}} + \frac{g_{m3,4}^2}{(\text{WL})_{3,4}} + \frac{g_{\text{Mb6,Mb2}}^2}{(\text{WL})_{\text{Mb6,Mb2}}}\right]} \tag{6}$$

where the transconductance of the corresponding transistors are denoted as g_m, the transistor output resistance as r_o, and the transimpedance gain of the amplifier as $A_{\rm vi}$. Equation (7) shows the gain of the current measuring unit (TIA) in the potentiostat. The inner common gate difference stage takes the difference in currents and produces a differential signal at the gates of transistor M10 and M12. Thus $V_{\rm differential}$ = Gain of $1^{\rm st}$ stage $\times$ (In+ − In−). The differential signal is buffered through the source follower stages M9 and M10, M11, and M12 and the amplifier through the differential pair M13–M16.

The input stages are optimized for noise, while maintaining a high gain and low power and a compact layout area. It is evident from equation (6) that at low frequencies the flicker noise dominates the overall noise and can be reduced by increasing the area of transistors M6, M7, M3, and M4. To achieve a satisfactory gain $r_{o3}\|r_{o1}$, $r_{o4}\|r_{o2}$ and r_{o16} need to be high. Thus, to optimize the first stage for noise and gain, current sources (M5–M7) were biased in strong inversion region (inversion coefficient, IC = 15 with an aspect ratio W/L = 5.3/5) and the active load (M3, M4) were biased in deep strong inversion region (IC = 50) with an aspect ratio W/L = 1/0.95. Biasing in strong inversion ensures the highest transistor output resistance, while moderate transistor sizing was chosen to optimize the performance of noise with layout area.

The input impedance demonstrates the current sinking capability of the transimpedance amplifier. From equation (5), a high g_m value would result in lower input impedance. As such, the common gate transistor, M1, M2, were biased in weak inversion region (IC = 0.1) with an aspect ratio W/L = 70/0.45 which allows higher g_m/I_d and the highest g_m possible for the bias current. In addition, it also minimizes the DC mismatch between the transistors, resulting in minimum DC offset, and ensures more room for the signal swing as $V_{\rm dsat}$ reaches its minimum value in weak inversion. The outermost differential stages (M8, M13–M16) were optimized for power, layout area, and output swing, and hence biased in moderate inversion region. M8 transistor was biased in moderate inversion region (IC = 3) with an aspect ratio W/L = 10/20 while M13, and M15 transistors were biased in moderate inversion region (IC = 0.2) with an aspect ratio W/L = 4/1 and M14, M16 transistors were biased in moderate inversion region (IC = 0.2) with an aspect ratio W/L = 2.52/10. The level shifters were biased in strong inversion region (IC = 15, W/L = 2.67/50) to achieve a high $r_{\rm ds}$ and a signal conversion gain close to unity. The current mirror isolating the potentiostat control unit from the transimpedance amplifier was optimized to operate in strong inversion region for the background current (Mb1-Mb3, IC = 30, W/L = 2.66/10 and Mb4–Mb5, IC = 30, W/L = 12.6/10).

D. Electrochemical Cell Voltage Swing

The applicability of a potentiostat to a particular application is dependent on the allowable cell voltage swing. A potentiostat capable of producing wide voltage swing is useful for detection of a number of electrochemical species which require different constant potentials at the reference terminal. However, for detecting glucose, the potentiostat needs only to be at a fixed $\rm V_{RE-WE}$ potential below 1 V (approximately −0.6 to −0.78 V for VACNF microelectrode). Compared to the differential potential control unit, a single ended potential control unit can sufficiently provide such voltage swing and at the same time results in reduced current consumption. The proposed potentiostat uses a 1.8 V rail-to-rail voltage and in the implemented circuit the voltage swing is limited to one transistor threshold below the highest rail (∼1.4 V) and above the lowest rail (∼450 mV) and is sufficient for VACNF based glucose sensing applications based on our experimental measurements.

E. Spurious Free Dynamic Range

The fundamental signal-to-spur ratio defines the quality of the signal and is an indication of amplifier distortion. The output signals of the difference-differential TIA can be represented as

$$V_{\rm out}{}^{+} = \sum_{n=1}^{\infty} k_n I_{\rm in}^n$$

$$V_{\rm out}{}^{-} = \sum_{n=1}^{\infty} k_n (-I_{\rm in})^n$$

$$V_{\rm out(difference-differential)} = V_{\rm out}{}^{+} - V_{\rm out}{}^{-} = \sum_{n=1,\rm odd}^{\infty} k_n (I_{\rm in})^n$$

$$V_{\rm out(single-ended)} = \sum_{n=1}^{\infty} k_n (I_{\rm in})^n \tag{8}$$

where $V_{\rm out+}$ is the output voltage due to the positive input current, $V_{\rm out-}$ is the output voltage due to the negative input current, and $V_{\rm out(difference-differential)}$ is the net output voltage of the difference-differential TIA topology and $V_{\rm out(single-ended)}$ is the output voltage of a single-ended TIA topology. Compared to a single ended amplifier topology the difference-differential amplifier suppresses even harmonics and has better dynamic performance.

IV. Experimental Results

The potentiostat potential control unit needs a high gain amplifier to regulate the current for a fixed potential difference. The amplifier was designed for 60 dB open loop gain. We have previously characterized VACNF microelectrodes for glucose sensing [11]. The electrochemical reduction current range is 0.2 to 2 μA for the glucose concentrations of 1 to 11 mM. The TIA thus needs to have rms noise lower than 100 nA. The blank solution generates a background current of 2 to 3 μA. For the 1 V output dynamic range, the TIA needs to have a gain of 100 dB to satisfy the full dynamic swing for the maximum electrochemical current of 10 μA. The TIA in the potentiostat is designed to meet these specifications. The potentiostat has been fabricated in a 0.18 μm commercially available CMOS process. The potential control unit and the difference-differential pair TIA have been characterized using SR785 dynamic spectrum analyzer and SR770 FFT network analyzer. Amplifiers A, A1, and A2 were implemented using folded cascode topologies with 60.2 dB open loop gain and 54.8° phase margin.

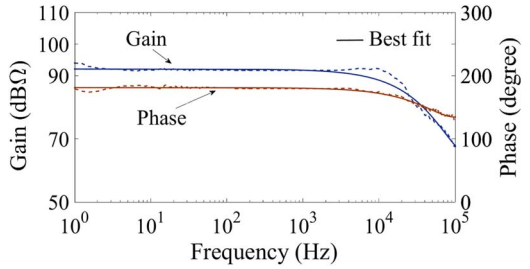

Fig. 6. (a) Measured gain and (b) phase response of the current measuring unit (difference-differential pair TIA).

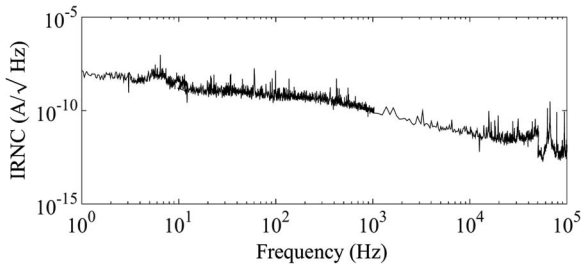

Fig. 7. Measured input referred noise current (IRNC) spectrum of the difference-differential pair TIA.

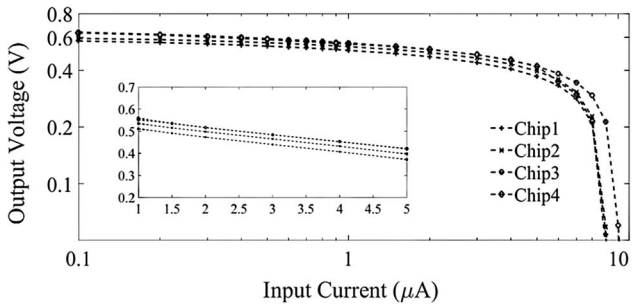

Fig. 8. Transfer characteristics of the current measuring unit (TIA), The inset shows that the 0.2–2 μA of electrochemical currents corresponding to 1–11 mM of physiological glucose concentrations adds with the 3 μA of background current and can swing 3 ± 2 μA on the linear region of the transfer plot.

Fig. 6 shows the experimentally measured gain and phase responses of the TIA. The data was averaged over 10 measurements and smoothed using a four-point moving averaging. The fit line corresponds to a single dominant pole, first order response. The transimpedance amplifier shows a gain of 92 dBΩ and a phase difference of less than 1° up to 5 kHz (Fig. 6). Fig. 7 shows the measured input referred noise spectrum of the implemented transimpedance amplifier without a low pass filter (LPF). The amplifier noise at 1 Hz is 8.1 nA/$\sqrt{\text{Hz}}$. The integrated noise is 0.69 μA over the equivalent noise bandwidth of 12.72 kHz and 71.8 nA with a 10 Hz LPF. Off-chip components can be added at the output of the TIA to implement a higher order LPF and reduce the high frequency spur. The experimentally measured transfer characteristics of the fabricated TIA chips are shown in Fig. 8. An SMU was used as the input current source and the output voltage was measured using a precision voltmeter. The experimental voltage transfer characteristics vary due to process variations in the open loop structure used in the design. The amplifier has a linear range from 500 nA to 7 μA. Fig. 9 shows the FFT of the output signal.

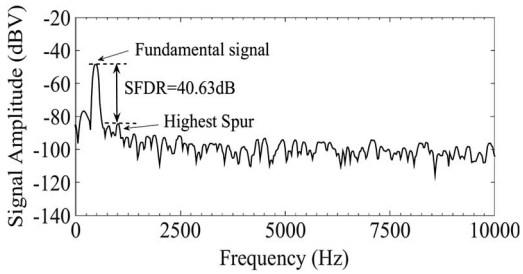

Fig. 9. FFT of the output signal of the current measuring unit (TIA).

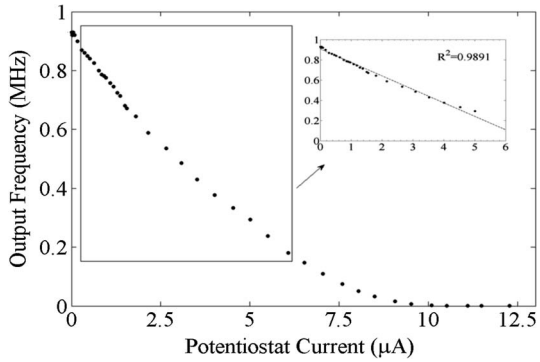

Fig. 10. Transfer characteristics of the integrated potentiostat.

The outer differential stage of the TIA is responsible for SFDR improvement by suppressing even harmonic components. A signal source was used to generate the voltage signal at the source terminals of M1 and M2. To determine the SFDR we assumed that the currents at the common-gate inputs create voltage ripples at the nodes Iin + and In−, and can be modeled by a voltage source in between these two nodes. For the designed TIA a 1 μA current results in 8.5 mV voltage ripple at Iin+ and In−. As such, a 20 mV source can generate currents close to the highest glucose concentration range ($\sim$2.35 μA). The FFT sampling rate was 50 kSa/s. A Hanning window was applied on the output signal and a total of 1000 points was acquired to generate the FFT plot. A Hanning window offers a bell-shaped weighting function and gives good spectral peak sharpness and reduced spectral leakage. The bell shaped spectrum resulted from use of the Hanning window. The frequency resolution was 25 Hz and the FWHM width of the fundamental peak was $\sim$200 Hz. The measured fundamental PSD is -48.75 dBV and the nearest strongest harmonic PSD is -89.37 dBV. The measured SFDR thus achieves a value of 40.62 dB. A common mode current is applied at the inputs and the output response of the TIA is measured to obtain the CMRR. The CMRR of the structure is 42 dB. The five-stage current starved VCO generates 500 Hz change in baseband signal frequency with 0.1 V change in VCO input or approximately 1 μA change in electrochemical current. The integrated transfer response of the potentiostat and the VCO is shown in Fig. 10. In the electrochemical cell, the solution resistance along with the charge transfer resistance at steady state results in a background offset current when no glucose is present. The sensor operates in amperometric mode with measurements taken after steady state is achieved. The current potentiostat setup uses VACNF sensors with a background current of 3 μA and a varying current

TABLE I
COMPARISON OF ELECTROCHEMICAL GLUCOSE SENSORS

Ref.	Sensor Type	Reaction Potential	Sensitivity	Detectable Glucose concentration range
[36]	GCNT/GOx/GAD	-0.44 V	2.47 μA mM^{-1} cm^{-2}	6.3 - 20.09 mM
[37]	GCE/CNT/Au/PDDA-GOx	-0.3 V	2.5 mA M^{-1}	0.5 - 5 mM
[38]	PPy-cMWCNT-GOx	+0.9 V	95 nA mM^{-1}	0.28* - 4 mM
This Work	VACNF-SU8/GOx/HRP	-0.78 V	50 - 200 nA mM^{-1} ** 89.035 μA mM^{-1} ***	1 - 11 mM** 0.4 - 4 μM ***

* According to calibration plot [38]
** Depending on fiber forest density on WE
*** According to calibration plot [10]

of 0.2 to 2 μA superimposed on it for the glucose concentrations of 1 to 11 mM. As such the background current sets up the DC operating point on the linear part in the TIA transfer plot (Fig. 8).

The potentiostatic setup is illustrated in Fig. 1. The potentiostat control unit is used to specify the potential difference between the reference and the working electrodes and was kept at a fixed potential to maintain the 0.781 V potential difference during the test. The glucose solution was mixed with 150 mM phosphate buffer saline solution (PBS) and poured into a well built around the VACNF working electrode. Ag/AgCl electrodes acting as the counter and the reference electrodes were also submerged into the solution. For a compact portable setup the Ag/AgCl reference and the counter electrodes can be fabricated on-chip by depositing Ag on a gold electrode and utilizing chronopotentiometry in 0.1 M KCl electroplating solution. The Ag/AgCl reference electrodes are used for accurate reference potential (non-polarizable electrode) in the electrochemical setup. However, the use of Ag/AgCl as the counter electrode can slow down electrochemical kinetics, which is a potential problem for real time measurements. This can be overcome by utilizing other inert counter electrode materials. However, the focus of this paper is to verify the VACNF/CMOS readout integrated sensor functionality. For a complete lab-on-a-chip system and practical implementation the electrodes can be fabricated as an integrated part of our VACNF fabrication process. The Ag/AgCl electrodes did not show degradation in performance throughout the experiments. Depending on the VACNF density on the WE the sensor demonstrates glucose detection sensitivities of 50 to 200 nA/mM [29]. Table I shows the performance of the amperometric sensor with other similar sensors [36]–[38].

This VACNF/CMOS sensor is mediator free. $Fe(CN)_6^{3-/4-}$ and $Ru(NH_3)_6^{2+/3+}$ are quasi reversible analytes that have been widely used and reported as the characterizing species in VACNF research [10], [30]. They indicate the electrochemical behavior of VACNF and surface activities in the electrolytic medium. We have chosen ruthenium hexamine trichloride ($Ru(NH_3)_6Cl_3$) for characterization verification of the surface

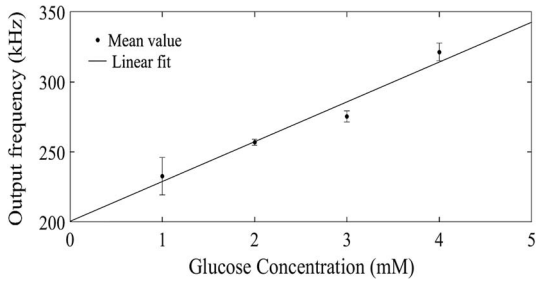

Fig. 11. Amperometric response of glucose solution in 0.1 M PBS with a 15 × 15 VACNF forest array (pitch 20 μm) on a 300 μm × 300 μm Ti at the VCO output (modulating signal).

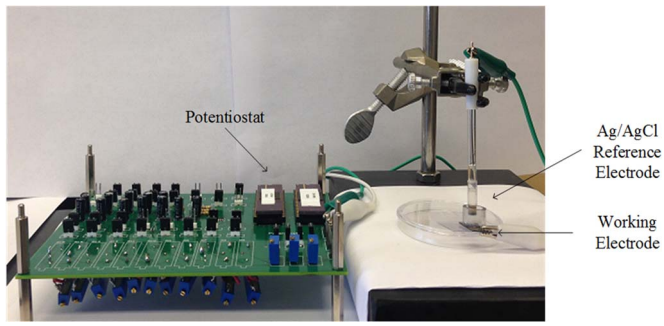

Fig. 12. Experimental test setup.

reactivity in electrochemical reactions of the VACNF sensors. The cyclic voltammetry of $Ru(NH_3)_6Cl_3$ in 0.1 M KCl solution with on-chip potentiostat shows oxidation and reduction peaks at -0.17 V and -0.24 V, respectively. The on-chip potentiostat integrated with a 30 × 30 VACNF forest array was tested in glucose solutions in 0.1 M PBS. High density VACNF forest saturates at higher concentration glucose due to diffusion limited current.

The 30 × 30 VACNF array can detect glucose with concentration up to 5 mM with high accuracy (Fig. 11) and the 20 × 20 array allows detection upto 11 mM [29]. The error bar reflects the variations of three measurements. Each concentration is prepared through weighing glucose and mixing with a calculated volume of de-ionized water, which can lead to greater sample preparation error than serial dilution resulting in a less linear response. Fig. 12 shows the experimental test setup. The current test setup is a two-chip integrated solution with off-chip biasing networks and Ag/AgCl reference electrode. The transimpedance amplifier consumes 44.5 μW of power, while the potential control unit of the current regulators [Fig. 4(b)] consumes 27.2 μW of power. The total power consumption of the potentiostat is 71.7 μW with the electrochemical cell. Table II shows a comparison of the proposed potentiostat with state-of-the-art topologies [14], [17], [18], [20], [39]. Compared to the potentiostats implemented in similar standard CMOS process, the current regulator based proposed potentiostat [Fig. 4(b)] is power and area efficient (consumes 39.83 μA from a 1.8 V supply, requires 0.0179 mm^2 of chip space, while providing a loop gain of 60.2 dB). The VACNF-SU8/GOx/HRP modified electrode improves the sensing sensivity of the monitoring system and demonstrates high amperometric detection sensitivity in glucose solution (200 nA/mM^{-1}).

TABLE II
COMPARISON OF POTENTIOSTAT PERFORMANCE

Work	**Yang *et al.* [17]**	**Roham *et al.* [18]**	**Martin *et al.* [14]**	**Nazari *et al.* [20]**	**Sohn *et al.* [39]**	**This Work**
Process	0.5 µm	0.5 µm	0.18 µm	0.35 µm	0.13 µm	0.18 µm
CE	Ti/Au	Not Reported	Pt wire	Not Reported	Not Reported	Ag/AgCl
RE	Ag/AgCl	Ag/AgCl	Calomel	Not Reported	Ag/AgCl	Ag/AgCl
WE	Ti/Au	Carbon fiber microelectrode	Pt	Not Reported	Pt	Vertically aligned carbon nanofiber microelectrode
WE Electrode Size	100 µm^2 (4 x 4 array)	3.5 µm radius (100 µm length)	10^{-6}- 10^{-4} cm^2 (7 x 2 array)	200 µm x 200 µm	Commercial Pt electrode	300 µm x 300 µm (30 x 30 array)
Chip Placement	Off-chip	Off-chip	On-chip	On-chip	Off-chip	Off-chip
Current Readout	Switched Capacitor	Sigma-delta modulator	Fully differential	Fully differential	Single ended	Difference-differential
Power Supply	5 V	2.6 V	1.8 V	3.3 V	3.3 V	1.8 V
Isupply	600 µA	22 µA	8.8 mA	16 µA (per OTA)	148 µA	39.83 µA
Sensor current detection range	6 pA - 10 µA	10 pA - 400 nA	Not Reported	100 pA - 60 nA	1 µA - 20 µA	500 nA - 7 µA
Potentiostat Core Area (mm^2)	1.68 (approx.)	0.06	0.45	0.04	0.036	0.0179

V. CONCLUSION

We have demonstrated a low-power compact potentiostat with a low-noise common gate difference-differential pair input TIA, a VCO and vertically aligned carbon nanofiber working electrodes. The performance of the sensor system was experimentally verified and tested in an amperometric setup with enzyme-functionalized VACNF working electrodes and Ag/AgCl reference and counter electrodes. The amperometric measurements showed glucose sensitivities ranging from 50 to 200 nA/mM based on fiber forests on the samples. The system requires 0.0179 mm^2 of chip area, consumes 71.7 μW of power from a 1.8 V supply and demonstrates 40.64 dB SFDR, and a detection range of 200 nA to 7 μA. The implemented VACNF-SU8/GOx/HRP electrode demonstrates a sensitivity of 200 nA/mM^{-1} in glucose solution. To the best of our knowledge, this is the first demonstrated potentiostat topology combined with VACNF nanostructures for glucose sensing. The current prototype sensor is used for a single-site sensor for glucose. However, the deterministic nature of VACNF growth allows for multi-site and multi-analyte sensing with appropriate enzyme functionalization, expanding the usefulness of the sensor for analyte detection.

ACKNOWLEDGMENT

The authors would like to thank Mr. C. K. Tailor for help with the LabVIEW data acquisition program. Carbon nanofiber growth and electron microscopy experiments were conducted at ORNL's Center for Nanophase Materials Sciences, which is a DOE Office of Science User Facility.

REFERENCES

[1] N. Tubiana-Rufi, J.-P. Riveline, and D. Dardari, "Real-time continuous glucose monitoring using Guardian RT: From research to clinical practice," *Diabetes Metabol.*, vol. 33, no. 6, pp. 415–420, 2007.

[2] S. K. Garg, H. K. Hoff, and H. P. Chase, "The role of continuous glucose sensors in diabetes care," *Endocrinol. Metabol. Clinics N. Amer.*, vol. 33, no. 1, pp. 163–173, 2004.

[3] S. K. Garg, H. K. Hoff, and H. P. Chase, "Standards of medical care in diabetes-2015: Summary of revisions," *Diabetes Care*, vol. 38 Suppl, p. S4, Jan. 2015.

[4] A. Heller and B. Feldman, "Electrochemical glucose sensors and their applications in diabetes management," *Chem. Rev.*, vol. 108, no. 7, pp. 2482–2505, 2008.

[5] J. D. Newman and A. P. Turner, "Home blood glucose biosensors: A commercial perspective," *Biosens. Bioelectron.*, vol. 20, no. 12, pp. 2435–2453, 2005.

[6] N. Oliver, C. Toumazou, A. Cass, and D. Johnston, "Glucose sensors: A review of current and emerging technology," *Diabetic Med.*, vol. 26, no. 3, pp. 197–210, 2009.

[7] P. Holt-Hindle, S. Nigro, M. Asmussen, and A. Chen, "Amperometric glucose sensor based on platinum-iridium nanomaterials," *Electrochem. Commun.*, vol. 10, no. 10, pp. 1438–1441, 2008.

[8] Y. Xian, Y. Hu, F. Liu, Y. Xian, H. Wang, and L. Jin, "Glucose biosensor based on Au nanoparticles-conductive polyaniline nanocomposite," *Biosens. Bioelectron.*, vol. 21, no. 10, pp. 1996–2000, 2006.

[9] J. Zang, C. M. Li, X. Cui, J. Wang, X. Sun, H. Dong, and C. Q. Sun, "Tailoring zinc oxide nanowires for high performance amperometric glucose sensor," *Electroanal.*, vol. 19, no. 9, pp. 1008–1014, 2007.

[10] A. B. Islam, F. S. Tulip, S. K. Islam, T. Rahman, and K. C. MacArthur, "A mediator free amperometric bienzymatic glucose biosensor using vertically aligned carbon nanofibers (VACNFs)," *IEEE Sensors J.*, vol. 11, no. 11, pp. 2798–2804, 2011.

[11] K. A. Al Mamun, F. S. Tulip, K. MacArthur, N. McFarlane, S. K. Islam, and D. Hensley, "Vertically aligned carbon nanofiber based biosensor platform for glucose sensor," *Int. J. High Speed Electron. Syst.*, vol. 23, no. 01n02, pp. 1–16, 2014.

[12] M. M. Ahmadi and G. Jullien, "Current-mirror-based potentiostats for three-electrode amperometric electrochemical sensors," *IEEE Trans. Circuits Syst. I, Reg. Papers*, vol. 56, no. 7, pp. 1339–1348, 2009.

[13] H. S. Narula and J. G. Harris, "VLSI potentiostat for amperometric measurements for electrolytic reactions," *IEEE Int. Symp. Circuits Syst.*, vol. 1, pp. I457–I460, 2004.

[14] S. M. Martin, F. H. Gebara, T. D. Strong, and R. B. Brown, "A fully differential potentiostat," *IEEE Sensors J.*, vol. 9, no. 2, pp. 135–142, 2009.

[15] R. F. Turner, D. J. Harrison, and H. P. Baltes, "A CMOS potentiostat for amperometric chemical sensors," *IEEE J. Solid-State Circuits*, vol. 22, no. 3, pp. 473–478, 1987.

[16] P.-A. Boutet and S. Manen, "Low power CMOS potentiostat for three electrodes amperometric chemical sensor," in *Proc. IEEE Faible Tension Faible Consommation*, 2011, pp. 15–18.

[17] C. Yang, Y. Huang, B. L. Hassler, R. M. Worden, and A. J. Mason, "Amperometric electrochemical microsystem for a miniaturized protein biosensor array," *IEEE Trans. Biomed. Circuits Syst.*, vol. 3, no. 3, pp. 160–168, 2009.

[18] M. Roham, D. P. Daberkow, E. S. Ramsson, D. P. Covey, S. Pakdeeronachit, P. A. Garris, and P. Mohseni, "A wireless IC for wide-range neurochemical monitoring using amperometry and fast-scan cyclic voltammetry," *IEEE Trans. Biomed. Circuits Syst.*, vol. 2, no. 1, pp. 3–9, 2008.

[19] K. A. Al Mamun, M. H. U. Habib, and N. McFarlane, "A low-power low-noise transimpedance amplifier for an integrated biosensing platform," in *Proc. IEEE Int. Midwest Symp. Circuits and Systems*, 2013, pp. 161–164.
[20] M. H. Nazari and R. Genov, "A fully differential CMOS potentiostat," in *Proc. IEEE Int. Symp. Circuits and Systems*, 2009, pp. 2177–2180.
[21] M. Razzaghpour, S. Rodriguez, E. Alarcon, and A. Rusu, "A highly-accurate low-power CMOS potentiostat for implantable biosensors," in *Proc. IEEE Biomedical Circuits and Systems Conf.*, 2011, pp. 5–8.
[22] W. Y. Chung, A. C. Paglinawan, Y. H. Wang, and T. T. Kuo, "A 600 μW readout circuit with potentiostat for amperometric chemical sensors and glucose meter applications," in *Proc. IEEE Conf. Electron Devices and Solid-State Circuits*, 2007, pp. 1087–1090.
[23] K. Murari, M. Stanacevic, G. Cauwenberghs, and N. V. Thakor, "Integrated potentiostat for neurotransmitter sensing," *IEEE Eng. Med. Biol. Mag.*, vol. 24, no. 6, pp. 23–29, 2005.
[24] A. Gore, S. Chakrabartty, S. Pal, and E. C. Alocilja, "A multichannel femtoampere-sensitivity potentiostat array for biosensing applications," *IEEE Trans. Circuits Syst. I, Reg. Papers*, vol. 53, no. 11, pp. 2357–2363, 2006.
[25] H. S. Narula and J. G. Harris, "A time-based VLSI potentiostat for ion current measurements," *IEEE Sensors J.*, vol. 6, no. 2, pp. 239–247, 2006.
[26] S. S. Ghoreishizadeh, C. Baj-Rossi, A. Cavallini, S. Carrara, and G. De Micheli, "An integrated control and readout circuit for implantable multi-target electrochemical biosensing," *IEEE Trans. Biomed. Circuits Syst.*, vol. 8, no. 6, pp. 891–898, 2014.
[27] J. Kim and W. Dunbar, "Nanopore-application CMOS potentiostat design with input parasitic compensation," *Electron. Lett.*, vol. 50, no. 8, pp. 578–579, 2014.
[28] M. R. Haider, S. K. Islam, S. Mostafa, M. Zhang, and T. Oh, "Low-power low-voltage current readout circuit for inductively powered implant system," *IEEE Trans. Biomed. Circuits Syst.*, vol. 4, no. 4, pp. 205–213, 2010.
[29] K. A. Al Mamun and N. McFarlane, "A CMOS potentiostatic glucose monitoring system for VACNF amperometric biosensors," in *Proc. IEEE Int. Symp. Circuits and Systems*, 2015, pp. 477–480.
[30] A. V. Melechko, V. I. Merkulov, T. E. McKnight, M. Guillorn, K. L. Klein, D. H. Lowndes, and M. L. Simpson, "Vertically aligned carbon nanofibers and related structures: Controlled synthesis and directed assembly," *J. Appl. Phys.*, vol. 97, no. 4, 2005, Art. no. 041301.
[31] K. A. A. Mamun, F. S. Tulip, K. MacArthur, N. McFarlane, S. K. Islam, D. Hensley, and I. I. Kravchenko, "A robust VACNF platform for electrochemical biosensor," in *Proc. IEEE Sensors Conf.*, 2013, pp. 1–4.
[32] P. Joshi, L. Zhang, Q. Chen, D. Galipeau, H. Fong, and Q. Qiao, "Electrospun carbon nanofibers as low-cost counter electrode for dye-sensitized solar cells," *ACS Appl. Mater. Interfaces*, vol. 2, no. 12, pp. 3572–3577, 2010.
[33] S. Siddiqui, P. U. Arumugam, H. Chen, J. Li, and M. Meyyappan, "Characterization of carbon nanofiber electrode arrays using electrochemical impedance spectroscopy: Effect of scaling down electrode size," *ACS Nano*, vol. 4, no. 2, pp. 955–961, 2010.
[34] R. De Boer and A. Van Oosterom, "Electrical properties of platinum electrodes: Impedance measurements and time-domain analysis," *Med. Biol. Eng. Comput.*, vol. 16, no. 1, pp. 1–10, 1978.
[35] D. M. Binkley, "Tradeoffs and optimization in analog CMOS design," in *Proc. Int. Conf. Mixed Design of Integrated Circuits and Systems*, 2007, pp. 47–60.
[36] A. P. Periasamy, Y.-J. Chang, and S.-M. Chen, "Amperometric glucose sensor based on glucose oxidase immobilized on gelatin-multiwalled carbon nanotube modified glassy carbon electrode," *Bioelectrochem.*, vol. 80, no. 2, pp. 114–120, 2011.
[37] Y.-L. Yao and K.-K. Shiu, "Direct electrochemistry of glucose oxidase at carbon nanotube-gold colloid modified electrode with poly(diallyldimethylammonium chloride) coating," *Electroanal.*, vol. 20, no. 14, pp. 1542–1548, 2008.
[38] Y. C. Tsai, S. C. Li, and S. W. Liao, "Electrodeposition of polypyrrole-multiwalled carbon nanotube-glucose oxidase nanobiocomposite film for the detection of glucose," *Biosensors Bioelectron.*, vol. 22, no. 4, pp. 495–500, Oct. 15, 2006.
[39] K. S. Sohn, S. J. Oh, E. J. Kim, J. M. Gim, N. S. Kim, Y. S. Kim, and J. W. Kim, "A unified potentiostat for electrochemical glucose sensors," *Trans. Electr. Electron. Mater.*, vol. 14, no. 5, pp. 273–277, 2013.

Khandaker A. Al Mamun (S'14) received the B.Sc. degree in electrical engineering from the Bangladesh University of Engineering and Technology, Dhaka, Bangladesh, in 2008.

Currently, he is working toward the Ph.D. degree in electrical engineering at the University of Tennessee (UT), Knoxville, TN, USA. From 2011 to 2015, he worked as a Graduate Teaching and Research Assistant at UT. His research interests are low-power analog and mixed signal circuit design, microfabrication and microelectrode design as well as sensor ASIC design and integration.

Syed K. Islam (S'91–M'94–SM'10) received the B.Sc. degree in electrical and electronic engineering from the Bangladesh University of Engineering and Technology, Dhaka, Bangladesh, and the M.S. and Ph.D. degrees in electrical engineering from the University of Connecticut, Storrs, CT, USA.

Currently, he is the James W. McConnell Professor in the Department of Electrical Engineering and Computer Science, University of Tennessee, Knoxville, TN, USA, where he is leading the research efforts of the Analog VLSI and Devices Laboratory. His research interests are design, modeling and fabrication of microelectronic/optoelectronic devices, molecular scale electronics and nanotechnology, biomicroelectronics, and monolithic sensors.

Dale K. Hensley received the Associate's degree in electrical engineering from Fountainhead College of Technology, Knoxville, TN, USA, in 1983.

Since August 1983, he has been involved in technical support for several research areas and user facilities, including ORELA, SMAC, and CNMS at Oak Ridge National Laboratory (ORNL), Oak Ridge, TN. Currently, he provides support for nanofabrication research with laboratory space management, tool ownership/training, synthesis, fabrication, and characterization. Since 2005, he has been a Controlled Synthesis Engineer in the Nanofabrication Research Laboratory Group, Center for Nanophase Materials Sciences (CNMS) Division, ORNL.

Nicole McFarlane (S'06–M'10) received the B.S. and M.S. degrees in electrical engineering from Howard University, Washington, DC, USA, in 2001 and 2003, respectively, and the Ph.D. degree in electrical engineering from the University of Maryland, College Park, MD, USA, in 2010.

In 2000 and 2001, she was an Electrical Engineering Intern at the Millstone Nuclear Power Plant, Waterford, CT, USA. Her research experience includes III–V-nitrides, information and power efficiency trade-offs in mixed-signal integrated circuit design, CMOS biosensors, and CMOS/MEMS integration for lab-on-a-chip technologies. Since 2010, she has been an Assistant Professor at the University of Tennessee, Knoxville, TN, USA, working on developing smaller and more efficient circuits and devices for sensing systems. Her research also focuses on novel circuit designs and device nanofabrication for applications in biological sensing and nuclear science.